Metabolic reprogramming of tumor-associated macrophages by collagen turnover promotes fibrosis in pancreatic cancer

Madeleine M. LaRue[a,b,1], Seth Parker[b,2] (iD), Joseph Puccini[b], Michael Cammer[c], Alec C. Kimmelman[b,d], and Dafna Bar-Sagi[b,3]

A hallmark of pancreatic tumors is their highly desmoplastic stroma composed of fibroblasts, immune cells, and a dense network of collagen fibers. Tumor-associated macrophages are one of the most abundant immune cell populations in the pancreatic tumor stroma. Their protumorigenic function has been attributed predominantly to their capacity to promote immune evasion and metastasis. Tumor-associated macrophages are also well known for their role in the remodeling of the stroma via collagen production and degradation, with the latter being mediated by mannose receptor (MRC1)-dependent endocytosis of collagen. Here we show that MRC1-mediated collagen internalization and subsequent lysosomal degradation by macrophages harboring a tumor-associated phenotype are accompanied by the accumulation of collagen-derived intracellular free amino acids and increased arginine biosynthesis. The resulting increase in intracellular arginine levels leads to the up-regulation of inducible nitric oxide synthase and the production of reactive nitrogen species. Furthermore, reactive nitrogen species derived from internalized and degraded collagen promotes a profibrotic phenotype in pancreatic stellate cells resulting in enhanced intratumoral collagen deposition. Overall, our findings identify a role for extracellular matrix remodeling in the functional modulation of tumor-associated macrophages via metabolic rewiring.

macrophage | collagen | fibrosis | stellate cell | pancreatic cancer

Pancreatic cancer is the third leading cause of cancer-related deaths in the United States and has a 5-y survival rate of 10% (1). Despite ongoing efforts to address these staggering statistics, pancreatic cancer remains a notoriously difficult disease to treat, likely due to late stage of diagnosis and resistance to both targeted and conventional therapeutics. A defining histopathological feature of pancreatic cancer is pronounced desmoplastic reaction characterized by the pervasive growth around the tumor of fibrotic tissue—comprised of fibroblasts, immune cells, and endothelial cells—embedded within dense extracellular matrix (ECM). The unique microenvironment generated by this robust fibroinflammatory response has been shown to significantly contribute to the clinical and biological aggressiveness of the disease by promoting tumor growth, metastasis, and therapeutic resistance (2–9).

The fibrous ECM of pancreatic tumors is principally produced by pancreatic stellate cells (PSCs). In a normal pancreas, stellate cells are quiescent and display a fat-storing phenotype. In a tumor-bearing pancreas, PSCs transform into an active myofibroblast-like phenotype (activated PSCs) in response to exposure to cytokines and growth factors secreted by cancer and immune cells in the tumor microenvironment (10–12). A hallmark of activated fibroblasts is their capacity to secrete elevated levels of ECM proteins, in particular collagens I and III, fibronectin, and laminin, the deposition of which leads to a pronounced interstitial fibrosis (13–15).

Tumoral fibrogenesis is a dynamic process by which the ECM is continuously remodeled through matrix synthesis, secretion, and degradation. Several protumorigenic effects have been attributed to ECM degradation (16, 17). These include the release of ECM-bound growth factors, which increases their bioavailability, the facilitation of cell migration and invasion, and the potentiation of leukocyte infiltration (16, 17). A key step in ECM remodeling is the degradation of collagens, which is mediated by two distinct catabolic pathways: 1) an extracellular pathway involving the cleavage of collagens by soluble and membrane-bound proteases produced by stromal and tumor cells, and 2) an endocytic pathway in which proteolytic fragments of collagens are internalized by mannose receptor (MRC1) in macrophages, and ENDO180 in fibroblasts, and subsequently degraded by lysosomal proteases (18, 19).

In the present study we report that MRC1-dependent collagen uptake and degradation by tumor-associated macrophages is accompanied by an increase in intracellular arginine

Significance

The highly desmoplastic and immunosuppressive microenvironment of pancreatic tumors is a major determinant of the aggressive nature and therapeutic resistance of pancreatic cancer. Therefore, improving our understanding of the mechanisms that regulate the composition and function of the pancreatic tumor microenvironment is critical for the design of intervention strategies for this devastating malignancy. This study identifies a modality for the reprogramming of tumor-associated macrophages involving collagen scavenging followed by a metabolic switch toward a profibrotic paracrine phenotype. These findings establish a molecular framework for the elucidation of regulatory processes that could be harnessed to mitigate the stroma-dependent protumorigenic effects in pancreatic cancer.

[1]Present address: Department of Microbiology and Immunology, Center for Immunology, University of Minnesota, Minneapolis, MN 55455.

[2]Present address: Department of Biochemistry and Molecular Biology, University of British Columbia, Vancouver, BC V6H 0B3, Canada.

[3]To whom correspondence may be addressed. Email: dafna.bar-sagi@nyulangone.org.

levels, which in turn results in the up-regulation of inducible nitric oxide synthase (iNOS) and the production of reactive nitrogen species (RNS). The macrophage-derived RNS promote, via a paracrine mechanism, the synthesis and extracellular deposition of collagens by PSCs leading to a pronounced increase in tumor fibrosis. These findings uncover a feedforward feedback mechanism that couples collagen synthesis and degradation, thereby contributing to ECM remodeling in pancreatic tumors.

Results

Macrophages Internalize Collagen via MRC1-Mediated Endocytosis. Macrophages are important mediators of the innate immune response, and depending on the cytokines and growth factors present in the local microenvironment, can adopt either pro- or anti-inflammatory phenotypes. Although it is now well appreciated that these phenotypic changes occur on a continuum, they can be broadly classified into two major states: an M1 classically activated state that is proinflammatory and an M2 alternatively activated state that is immunosuppressive. M1 macrophages are activated by immune-stimulating factors, including interferon-γ (IFN-γ), lipopolysaccharide (LPS), and granulocyte macrophage colony stimulating factor. They are characterized by the production of high levels of proinflammatory cytokines, reactive nitrogen and oxygen intermediates, and promotion of type 1 helper T cell (Th1) responses. Conversely, M2 macrophages are activated by factors that dampen activated immune responses and promote wound healing, including interleukin (IL)-4, IL-10, and IL-13 and transforming growth factor-β (TGF-β). They typically display immune-suppressive capabilities and are considered to be tumor promoting (20–22).

To investigate the relative roles of M1 and M2 macrophages in ECM remodeling via collagen degradation, we first sought to compare their collagen uptake capacities. To this end, bone marrow-derived macrophages (BMDMs) were polarized to an M1-like state (hereafter, referred to as M1) using LPS, or to an M2-like state (hereafter, referred to as M2) using IL-4, and incubated with Oregon Green (OG)-conjugated gelatin (partially degraded collagen). Gelatin uptake was quantified by measuring the fluorescence intensity of OG-labeled intracellular punctae. M2 macrophages displayed a higher level of gelatin internalization relative to either M0 (unstimulated) or M1 (LPS-polarized) macrophages (Fig. 1*A*). The preferential uptake of gelatin by M2 macrophages was correlated with a higher expression of *Mrc1* (Fig. 1*A*) independent of gelatin addition (*SI Appendix,* Fig. S1*A*), suggesting that the major route of collagen uptake in M2 macrophages is via MRC1-mediated internalization. This postulate was validated by demonstrating that gelatin uptake was significantly reduced by small-interfering RNA (siRNA)-mediated knockdown of *Mrc1* in M2 macrophages (Fig. 1*B* and *SI Appendix,* Fig. S1 *A–C*) and could not be detected in M2 macrophages derived from *Mrc1* knockout mice (Fig. 1*C* and *SI Appendix,* Fig. S1*D*). In addition, the increase in collagen uptake was preferentially observed under polarization conditions that induce the up-regulation of *Mrc1* (*SI Appendix,* Fig. S1*E*).

To further assess collagen uptake mechanisms by macrophages in the setting of pancreatic tumors, pancreatic cancer cells derived from *Kras*$^{LSL-G12D/+}$*;p53*$^{LSL-R172H/+}$*;Pdx-1-Cre* mice (*KPC*) were implanted subcutaneously into wild-type or *Mrc1* knockout mice. Following intratumoral injection of OG-gelatin, tumors were harvested and processed for fluorescence microscopy. Tumor-associated macrophages from *Mrc1* knockout mice were found to be defective in gelatin uptake (Fig. 1*D*), affirming the essentiality of this receptor for macrophage-mediated remodeling of tumor-associated ECM.

MRC1-Dependent Collagen Internalization Up-Regulates iNOS Expression in M2 ARG1$^+$ Macrophages. Given the predominance of M2 macrophages in the tumor microenvironment (20–22), we next sought to investigate the effects of MRC1-dependent gelatin uptake on the inflammatory phenotype of M2-polarized macrophages by assessing the expression levels of iNOS and arginase 1 (ARG1), well-established markers of pro- and anti-inflammatory macrophages, respectively (23, 24). The addition of gelatin was sufficient to induce a marked up-regulation of *iNos* transcripts and protein, as well as an increase in *Arg1* transcription (Fig. 2 *A* and *B*). Moreover, flow cytometry analysis revealed a pronounced gelatin-dependent increase in the fractions of M2-polarized macrophages that display the simultaneous expression of ARG1 and iNOS (Fig. 2*C* and *SI Appendix,* Fig. S2*A*). These observations suggest that the exposure of M2 macrophages to gelatin can lead to the acquisition of a macrophage phenotype that harbors both M1 and M2 markers, hereafter referred to as ARG1$^+$iNOS$^+$ phenotype. Significantly, the presence of this ARG1$^+$iNOS$^+$ macrophage population was detected in vivo both in murine models of pancreatic cancer and in human pancreatic ductal adenocarcinoma (PDA). Specifically, in an autochthonous model of PDA (*Kras*$^{LSL-G12D/+}$*;p53*$^{LSL-R172H/+}$*;p48-Cre*$^{tg/+}$ genetically engineered mouse model, hereafter, *KPC* GEMM) ~3% of macrophages (CD45$^+$F4/80$^+$Ly6C$^-$) were double-positive for ARG1 and iNOS (Fig. 2*D*). In addition, in orthotopic pancreatic tumors generated by the implantation of *KPC* pancreatic cancer cells into the pancreata of wild-type syngeneic mice, ~4.5% of CD45$^+$F4/80$^+$Ly6C$^-$ cells exhibited this ARG1$^+$iNOS$^+$ phenotype (Fig. 2*D* and *SI Appendix,* Fig. S2*B*). Finally, multiplex immunohistochemical analysis of human PDA sections demonstrated that ~1.5% of CD68$^+$CK19$^-$ cells exhibit an ARG1$^+$iNOS$^+$ phenotype (Fig. 2*E*). Together, these results validate the existence of ARG1$^+$iNOS$^+$ macrophages in the pancreatic tumor microenvironment.

We next asked whether the gelatin-induced ARG1$^+$iNOS$^+$ phenotype in vivo is MRC1-dependent. siRNA-mediated knockdown of *Mrc1* in M2-polarized macrophages led to a significant reduction in the capacity of gelatin to induce the up-regulation of iNOS in vitro (Fig. 2 *A* and *B*). Likewise, gelatin-mediated increase in *Arg1* expression was lessened by *Mrc1* knockdown in vitro (Fig. 2*A*). Thus, we concluded that MRC1 is required for the acquisition of ARG1$^+$iNOS$^+$ phenotype upon exposure to gelatin. Consistent with this interpretation, in orthotopic tumors this phenotype was more prevalent in macrophages that are MRC1^{high}, as determined by CD206 expression, in comparison to macrophages that are MRC1^{low} (Fig. 2*F* and *SI Appendix,* Fig. S2*C*).

Arginine Metabolism Links MRC1-Dependent Collagen Internalization and Degradation to Macrophage Phenotype Reprogramming. In addition to their roles in dictating the polarization state of macrophages (23, 24), iNOS and ARG1 are also the primary arginine metabolism enzymes in these cells. ARG1 hydrolyzes arginine to ornithine and urea where iNOS converts arginine to nitric oxide (NO) and citrulline (25, 26). Furthermore, it has been shown that arginine availability regulates iNOS and ARG1 expression, and that the arginase pathway limits arginine availability for NO synthesis (24, 27). As the interaction of gelatin with MRC1 is followed by its internalization and lysosomal degradation, we reasoned that the generation of free arginine through this degradation process could serve as the mechanism by which gelatin up-regulates the expression of *Arg1* and *iNos* in M2-polarized macrophages. To
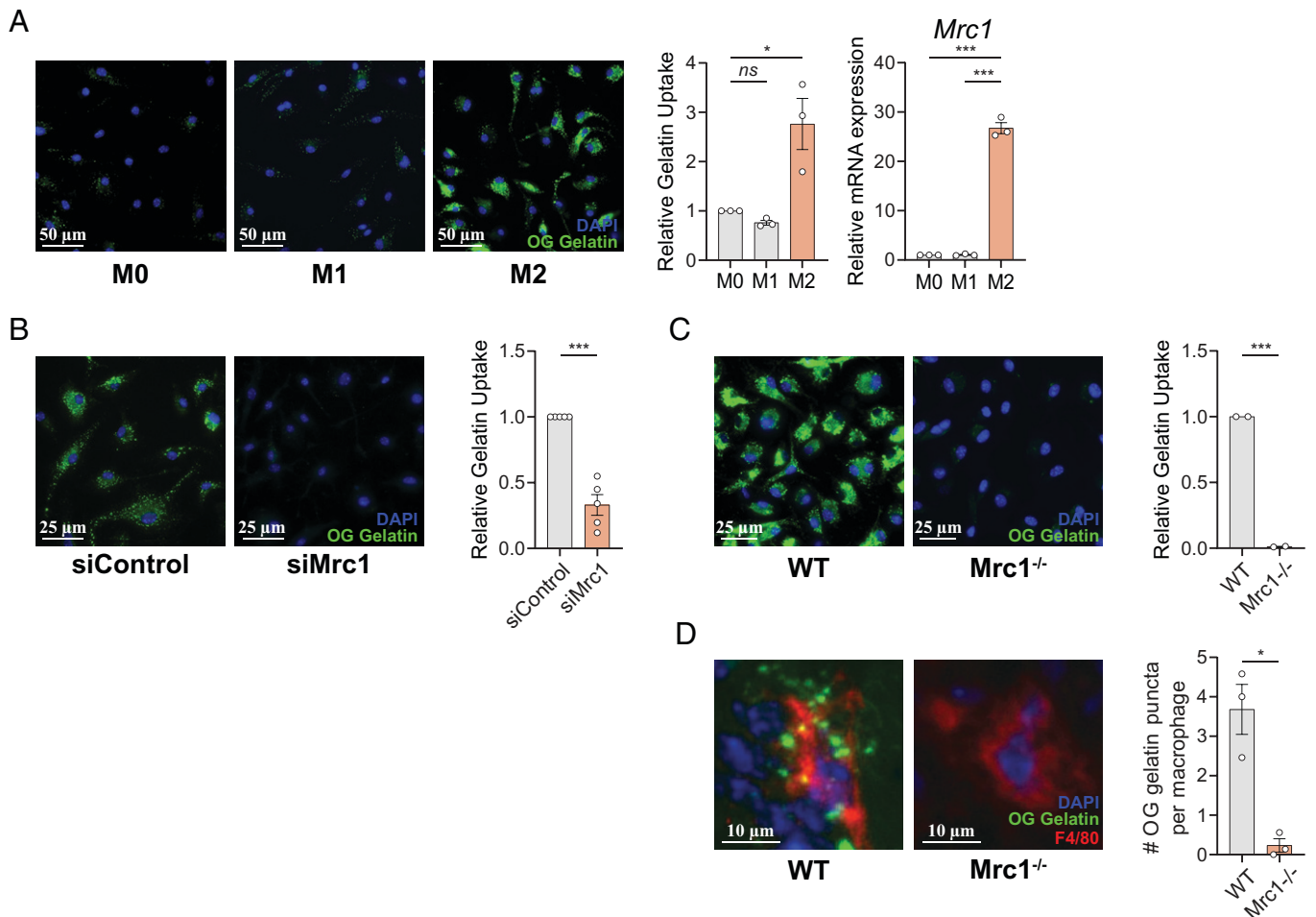
Fig. 1. Macrophages internalize and degrade collagen via Mrc1-mediated endocytosis. (*A*) Representative fluorescence microscopy images (*Left*) and quantification (*Center*) of BMDMs from C57BL/6 mice either unstimulated (M0) or treated with LPS (M1) or IL-4 (M2) fed OG-gelatin. (*Right*) Analysis of mRNA expression by quantitative PCR of *Mrc1* normalized to a *GAPDH* housekeeping gene and presented relative to M0. (*B*) Representative fluorescence microscopy images (*Left*) and quantification (*Right*) showing IL-4–treated BMDMs (M2) transfected with siRNA targeting Mrc1 or control siRNA and fed OG-gelatin. (*C*) Representative fluorescence microscopy images (*Left*) and quantification (*Right*) of IL-4–treated BMDMs (M2) from mannose receptor (*Mrc1*) knockout mice or wild-type littermate controls fed OG gelatin. Data represents average uptake index within BMDMs from two mice sampled, with at least $n = 3$ technical replicates per mouse. (*D*) KPC pancreatic cells were injected subcutaneously into flanks of *Mrc1* knockout mice or wild-type littermate controls. At ~300 mm^3, tumors were injected with OG gelatin (green) and uptake by F4/80$^+$ cells (red) was analyzed by indirect immunofluorescence of tumor cryosections. Nuclei are labeled with DAPI (blue). Graph (*Right*) represents the average number of OG gelatin puncta observed in randomly selected F4/80$^+$ cells per tumor sampled (50 macrophages per tumor). Quantification of all fluorescent images are presented in arbitrary units and relative to values obtained for control conditions (untreated, DMSO, or wild-type). For all graphs, values are mean ± SE for at least $n = 3$ independent experiments, unless otherwise noted. Statistical significance was determined using a Student's *t* test. *$P < 0.05$; ***$P < 0.0001$; ns, not significant.

test this idea, we first investigated the dependence of the observed ARG1$^+$iNOS$^+$ phenotype on lysosomal degradation of gelatin using Bafilomycin-A (Baf-A), an inhibitor of lysosomal acidification that is required for the degradation of macromolecules. The gelatin-induced increase in *Arg1* and *iNos* expression was significantly attenuated when M2-polarized macrophages were treated with Baf-A (Fig. 2*G*). Moreover, metabolomics analysis demonstrated that exposure of M2-polarized macrophages to gelatin was accompanied by an increase in intracellular arginine pool size, which was significantly reduced by *Mrc1* knockdown (Fig. 2*H*).

Together, these results indicate that MRC1-mediated uptake and degradation of gelatin could lead to the accumulation of intracellular free arginine. In principle, this might occur through the generation of arginine itself as a degradation product of gelatin or through the generation of other amino acids (e.g., proline and glutamine) that can be subsequently metabolized to arginine (Fig. 2*I*). To distinguish between these possibilities, we used α-methyl-DL-aspartic acid (MDLA), an inhibitor of the key regulatory enzyme of arginine biosynthesis, argininosuccinate synthase 1

(ASS1) (Fig. 2*I*). MDLA treatment of M2-polarized macrophages resulted in the reduction of gelatin-induced expression of *iNos*, indicating that intracellular arginine biosynthesis pathways drive in part the ARG1$^+$iNOS$^+$ macrophage phenotype (Fig. 2*I*). Among these, the pathway involving the conversion of proline to ornithine might be of particular relevance because of the uniquely high content of proline in gelatin. Of note, the utilization of intracellular proteolytic processing of collagen as a source for arginine could be of particular relevance, given recent evidence that arginine is the most depleted amino acid in the tumor interstitial fluid of PDA tumors (28).

Collagen-Internalizing Macrophages Produce RNS That Promote a Profibrotic Phenotype in Pancreatic Stellate Cells In Vitro. RNS are a large, diverse group of signaling molecules generated by the interaction of NO with other reactive species in the environment. RNS production has been linked to alterations in signal transduction pathways through a spectrum of posttranslational modifications that these species can engender (29, 30). Since NO is a product of iNOS and the latter is
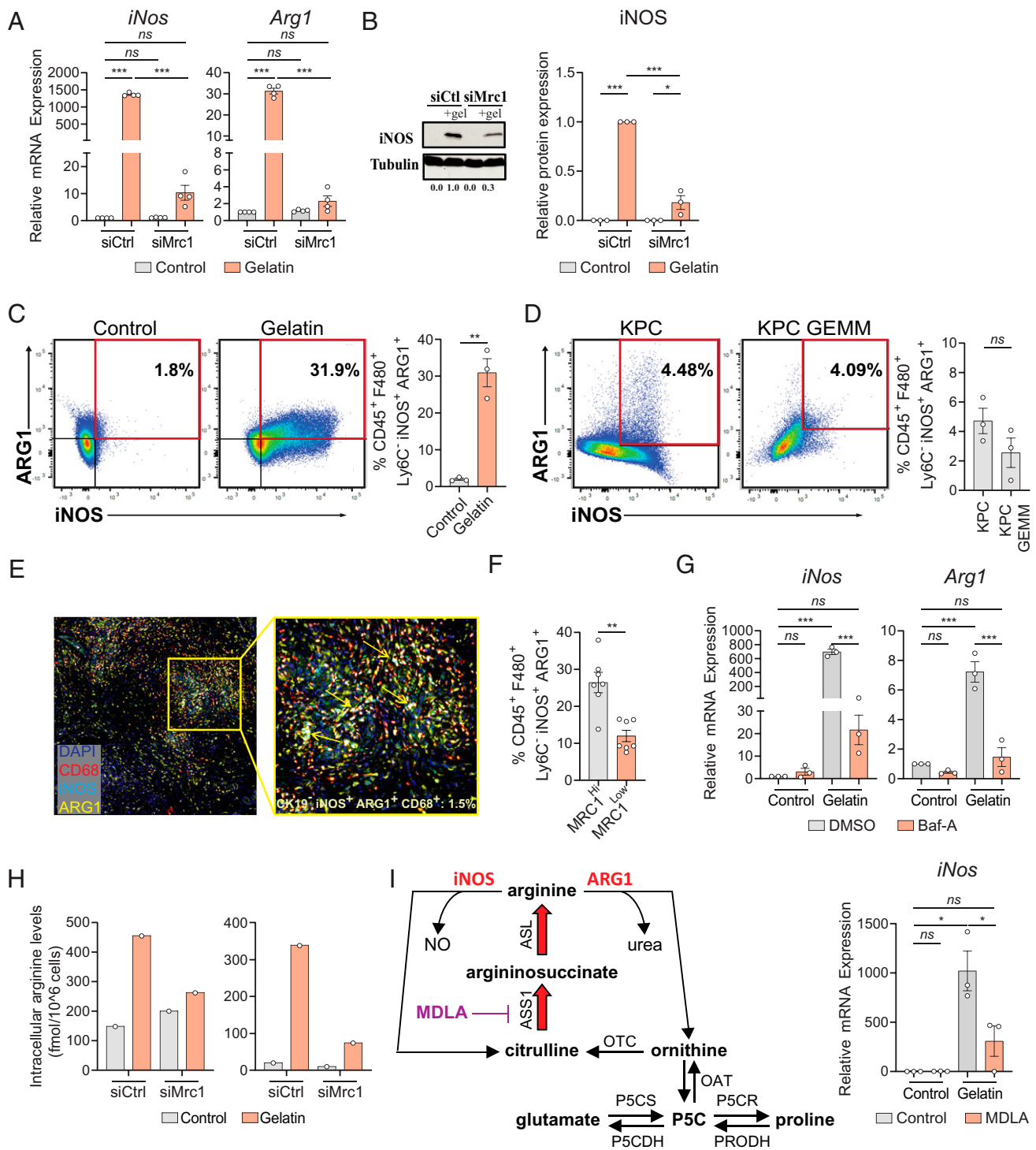
Fig. 2. Collagen uptake and degradation augments intracellular arginine bioavailability and enhances expression of arginine metabolism enzymes in macrophages. (*A*) Analysis of mRNA expression by quantitative PCR of *iNos* (*Left*) or *Arg1* (*Right*) in IL-4–treated BMDMs transfected with siRNA targeting control (siCtl) or Mrc1 (siMrc1) fed 1% gelatin. (*B*) Representative Western blot (*Left*) and quantification (*Right*) of iNOS protein expression in IL-4–treated BMDMs transfected with siRNA targeting Mrc1 (siMrc1), or control (siCtl), and fed 1% gelatin (*n* = 3). Tubulin serves as loading control. Data were normalized to siCtl + gelatin condition. (*C* and *D*) Flow cytometry analysis showing percent CD45$^+$F4/80$^+$Ly6C$^-$iNOS$^+$ARG1$^+$ cells from (*C*) IL-4–treated BMDMs without (control) or with 1% gelatin or (*D*) 2-wk-implanted KPC orthotopic pancreatic tumors and 3-mo-old KPC GEMM mouse pancreata. Representative flow cytometry plots (*Left*) and quantification (*Right*, *n* = 3) are shown. (*E*) CD68$^+$iNOS$^+$ARG1$^+$ macrophages in human PDAs by OPAL high-throughput multicolor IHC analysis. 20x magnification (*Right*). Indicated box (*Left*) is enlarged. Arrows identify several clusters of CD68$^+$iNOS$^+$ARG1$^+$ macrophages. Image is 1 representative of ~180 from three tumors analyzed. (*F*) Flow cytometry analysis showing percent CD45$^+$F4/80$^+$Ly6C$^-$iNOS$^+$ARG1$^+$ cells in MRC1^{high} versus MRC1^{low} macrophage populations in 2-wk-implanted KPC orthotopic pancreatic tumors. (*G*) Analysis of mRNA expression of *iNos* (*Left*) and *Arg1* (*Right*) by quantitative PCR in IL-4–treated BMDMs treated as shown and normalized to DMSO control. (*H*) GC-MS metabolomics analysis showing intracellular arginine levels (fmol per 1 × 10^6 cells) in IL-4–treated BMDMs transfected with siMrc1 or siCtl and treated with 1% dialyzed gelatin or PBS (control). Absolute values of arginine are shown due to interexperimental variability in baseline intracellular levels of arginine observed in M2 macrophages. (*I, Left*) Diagram of intracellular arginine biosynthesis and target of MDLA inhibition. (*Right*) Analysis of mRNA expression of *iNos* by quantitative PCR in IL-4–treated BMDMs treated as shown and normalized to control. For all graphs, values are mean ± SE for at least *n* = 3 independent experiments. All mRNA data were normalized to GAPDH housekeeping gene during analysis. Statistical significance was determined using a Student's *t* test or one-way ANOVA test. Adjusted *P* values for two group comparisons are plotted. *$P < 0.05$; **$P < 0.001$; ***$P < 0.0001$; ns, not significant.

highly up-regulated by gelatin internalization and degradation (Fig. 2 *A*, *B*, and *G*), we postulated that gelatin scavenging by macrophages could lead to the production of RNS. To test this postulate, conditioned medium from M2 polarized macrophages exposed to gelatin was collected and the levels of the NO metabolites nitrate, nitrite, and peroxynitrite were measured. Confirming our prediction, gelatin uptake led to a pronounced increase in the production of RNS (Fig. 3 *A* and *B*). The levels of RNS produced were generally similar to those produced by treating M2-polarized macrophages with LPS, a known stimulator of NO production through Toll-like receptor-mediated increase in iNOS expression. Furthermore, the gelatin-induced increase in RNS production was ablated by treatment with the iNOS inhibitor 1400W, implicating iNOS as an essential mediator of this response (Fig. 3 *A* and *B*).

The reaction of RNS with biomolecules has been shown to be involved in the regulation of diverse physiological and pathophysiological processes. Since excessive deposition of ECM is a cardinal feature of pancreatic tumors, the reported role of RNS in promoting hepatic fibrogenesis through the activation of hepatic stellate cells was of particular interest (31). We therefore asked whether RNS derived from ARG1⁺iNOS⁺ macrophages could induce an ECM-producing phenotype in the pancreas. To this end, immortalized PSCs were cultured in conditioned medium from macrophages that were incubated with gelatin in the presence or absence of the iNOS inhibitor 1400W. In response to RNS-containing conditioned medium from gelatin-fed macrophages, PSCs acquired a profibrotic phenotype as measured by the enhanced transcription of ECM-remodeling genes (*αSma*, *Ctgf*, and *Cdh10*) and collagen synthesis genes (*Hsp47*, *Col1a1*, *Col2a1*, *Col3a1*, and *Col4a1*) (Fig. 3*C*). The observed transcriptional effects were retained when heat-denatured conditioned medium was used (*SI Appendix*, Fig. S3*A*), ruling out the potential role of macrophage-derived signaling proteins, and could be replicated by treating PSCs with DPTA-NONOate, an NO donor, indicating a direct role for NO generation in conferring the observed phenotype (Fig. 3*C*). Of note, similar transcriptional responses were observed in an experiment using primary PSCs isolated from healthy pancreata of wild-type mice (*SI Appendix*, Fig. S3*B*), excluding potential confounding effects of PSC immortalization. Importantly, the RNS-mediated transcriptional reprogramming of PSCs is accompanied by increases in the levels of intracellular (Fig. 3*D*) and extracellular (Fig. 3*E*) collagen type 1 (COL1A1), the primary fibrillar collagen subtype in the pancreatic tumor microenvironment. Together, these observations indicate that collagen uptake by macrophages and the resulting production of RNS could promote the accumulation of activated ECM-producing PSCs.

PSCs Exposed to RNS Enhance Pancreatic Intratumoral Fibrosis In Vivo. Enhanced intratumoral fibrosis has been shown to promote tumor growth in several ways, including augmenting metastasis and invasion capabilities of cancer cells, and acting as a physical barrier to infiltrating tumor cell cytotoxic immune cells and chemotherapeutics (32). Therefore, we sought to determine whether the RNS-mediated activation of PSCs could enhance intratumoral fibrosis in vivo. To this end, PSCs treated with conditioned medium from gelatin-reprogrammed ARG1⁺iNOS⁺ macrophages were coimplanted subcutaneously with *KPC* pancreatic cancer cells into the rear flanks of NCr nude mice. After 2 wk, tumors were harvested and collagen deposition was assessed by Trichrome and Picrosirius red staining. A substantial increase in the density of

intratumoral collagen fibers was observed selectively in tumors derived from *KPC* cells coimplanted with conditioned medium-treated PSCs (Fig. 4 *A* and *B*). This increase was reversed when the coimplanted PSCs were treated with conditioned medium from macrophages treated with 1400W, which inhibits RNS production by macrophages and induction of PSC profibrotic phenotype (Fig. 4 *A* and *B*). No significant differences between the number of mesenchymal stromal cells was observed across the different coimplantation conditions, ruling out the possibility that the observed increase in fibrosis is due to expansion of collagen-producing cells (Fig. 4*C*). Collectively, these data demonstrate that RNS-mediated cross talk between ARG1⁺iNOS⁺ macrophages and PSC can contribute to the desmoplastic reaction in pancreatic tumors. The potential relevance of this cross-talk to tumor growth is suggested by the observation that the tumor-promoting effect of cotransplanted PSCs that were treated with conditioned medium was reduced when the cotransplanted PSCs were derived from conditioned medium that included 1400W (*SI Appendix*, Fig. S4).

Discussion

It is now widely recognized that tumor-associated ECM plays a fundamental role in dictating the phenotypes and functions of both tumor and stromal cells (33). Therefore, an understanding of the molecular mechanisms underlying the communication between the ECM and tumor resident cells is critical for overcoming ECM-mediated therapeutic barriers. In this study, we identify a role for collagen, the major constituent of tumor ECM, in the regulation of macrophage phenotype via metabolic reprogramming. This cross-talk could contribute to specific pathologies associated with pancreatic cancer as well as other tumor types that harbor collagen-rich tumor microenvironment.

The existence of pathways for collagen uptake and intracellular degradation are not unique to macrophages. Pancreatic tumor cells have been shown to possess the capacity to internalize collagen via macropinocytosis and an additional uptake mechanism likely mediated by the uPAR-associated protein/ENDO180 (34). ENDO180-mediated uptake of collagen has been also documented in pancreatic cancer-associated fibroblasts (CAFs) (35). Despite sharing a common route of collagen entry, these three cell types display differential metabolic effects resulting from collagen catabolism. Whereas in macrophages, as shown in this study, the products of collagen degradation up-regulate arginine biosynthesis, in tumor cells collagen-derived proline fuels TCA cycle metabolism (34), and in CAFs, collagen degradation supplies amino acid precursors for branched-chain amino acid metabolism (35). These differences highlight the broad and versatile role of collagen scavenging in regulating tumor metabolic flexibility.

A salient feature of the collagen scavenging-dependent metabolic reprogramming of macrophages described in this study is the up-regulation of iNOS and the resulting production of RNS. Our findings that this facet of the metabolic reprogramming promotes a profibrinogenic PSC phenotype are in agreement with earlier studies demonstrating a role for RNS in tissue repair processes associated with fibrosis (31, 36, 37). Furthermore, pharmacological or genetic NOS inhibition has been shown to decrease collagen deposition in tissues (38, 39). The precise mechanisms by which macrophage-derived RNS stimulate a fibrogenic response in PSCs remains to be determined. However, the observation that this response encompasses the transcriptional up-regulation of multiple genes that contribute to collagen biosynthesis and deposition is consistent
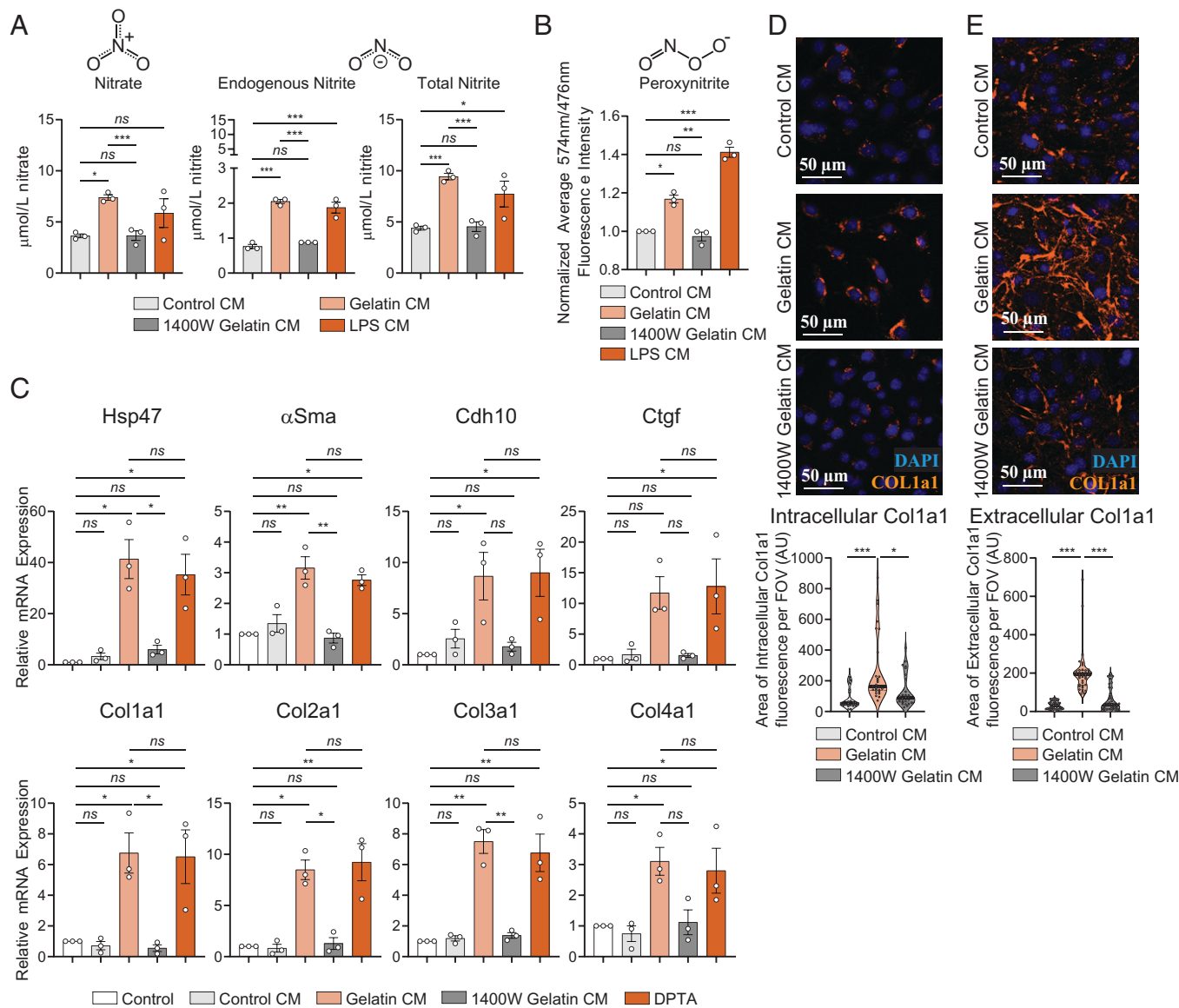
Fig. 3. Macrophages produce reactive nitrogen species during collagen uptake and degradation that promote a profibrotic phenotype in pancreatic stellate cells. (*A*) Total nitrite (μmol/L), endogenous nitrite (μmol/L), and nitrate (μmol/L) measured using a colorimetric NO Detection Kit in cell culture supernatant collected from untreated (Control CM), gelatin-fed (Gelatin CM), 1400W-treated and gelatin-fed (1400W Gelatin CM), or LPS-treated (LPS CM) macrophages. (*B*) Peroxynitrite production by macrophages determined by quantifying the 574 nm/476 nm fluorescence intensity ratio of a peroxynitrite-specific ratiometric probe, normalized to control. Ten randomly selected cells were analyzed per frame. Each frame was averaged per condition and normalized to control. (*C*) Relative mRNA expression of *Hsp47*, *αSma*, *Ctgf*, *Cdh10*, *Col1a1*, *Col2a1*, *Col3a1*, and *Col4a1* in murine PSCs measured by qPCR analysis and normalized to control. All mRNA data were normalized to a housekeeping gene, GAPDH, during analysis. (*D*) Intracellular and (*E*) extracellular immunofluorescence staining of COL1A1 (orange) and nuclei (blue) in conditioned medium from IL-4–treated BMDMs fed with PBS (Control CM), 1% gelatin (Gelatin CM), or 1400W + 1% gelatin (1400W Gelatin CM). All fluorescent images quantified in arbitrary units and presented relative to values obtained for control. For qPCR graphs, values are mean ± SE for at least *n* = 3 independent experiments. For immunofluoresence analysis, each dot represents quantification in one field of view, *n* = 2 independent experiments. Statistical significance was determined using a one-way ANOVA test. Adjusted *P* values for two group comparisons are plotted. *$P < 0.05$; **$P < 0.001$; ***$P < 0.0001$; ns, not significant.

with the engagement of a regulatory circuit that controls collagen production. Indeed, RNS have been shown to augment the TGF-β signaling pathway (40, 41), a core pathway that orchestrates matrix synthesis in fibroblasts including PSCs (42, 43). Of note, the RNS peroxynitrite has been implicated in TGF-β–mediated differentiation of fibroblasts to matrix-producing myofibroblasts (44). Peroxynitrite is the product of the reaction of NO with superoxide radical (45). Unique among other RNS, peroxynitrite mediates the posttranslational modification of proteins via nitration with tyrosine residues being the major target of this modification (45). Under some conditions, protein nitration has been shown to be not readily reversible, indicating the potential for this posttranslational modification to

engender alterations of cellular processes that are more stable than most other redox signals. The protracted time frame of our in vivo cotransplantation experiments indicate that PSCs subjected to macrophage-derived RNS, including peroxynitrite, might undergo a durable reprogramming. Given the increasing appreciation of the importance of unique PSC subsets in the pathogenesis of pancreatic cancer (46, 47), this RNS-mediated cross-talk mechanism could have a significant impact on disease development and progression.

Increased deposition of fibrillar collagen is a defining pathology of pancreatic tumors. A number of tumor-promoting processes have been directly linked to collagen fibril density (48). Of particular relevance are recent findings indicating that the
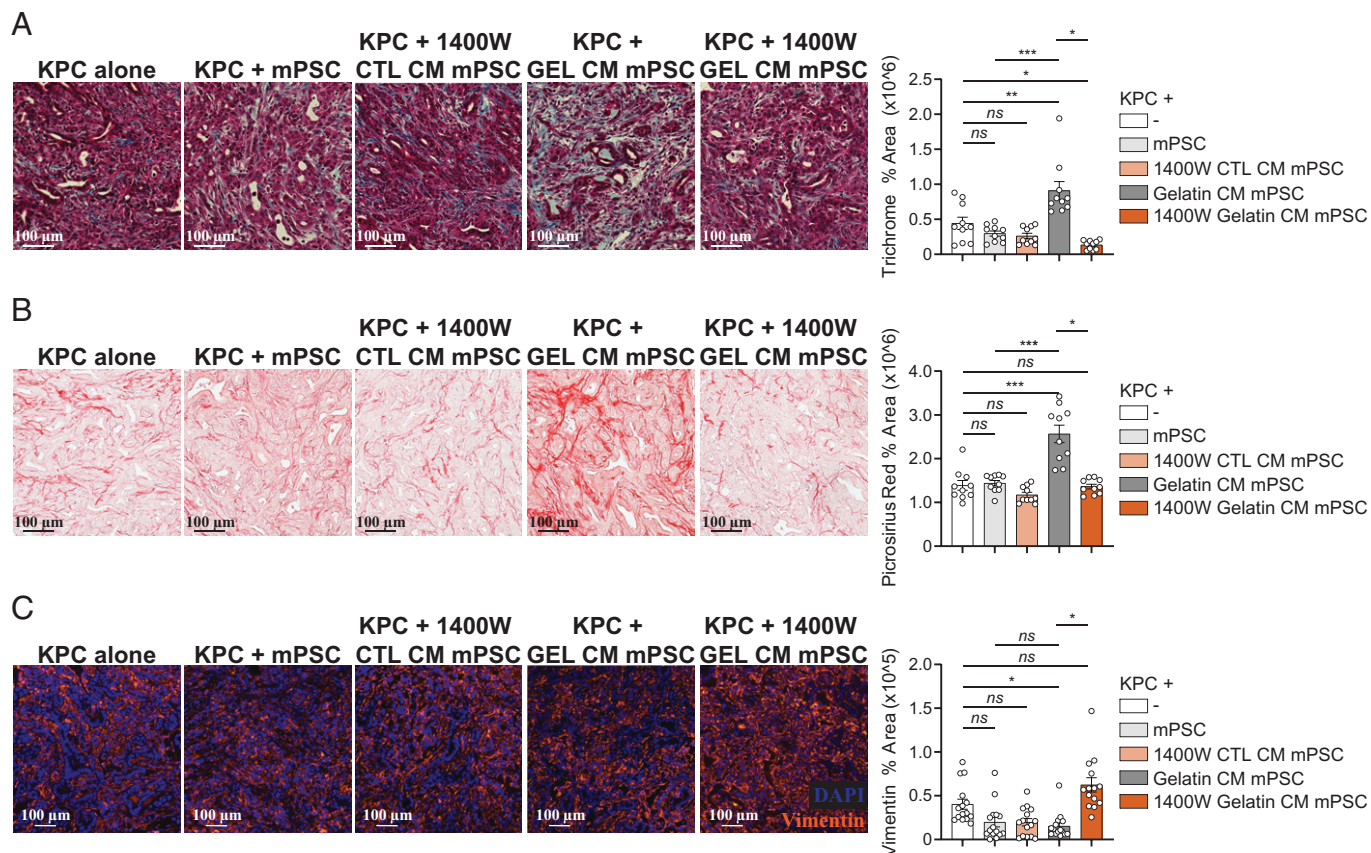
Fig. 4. PSCs exposed to macrophage-derived reactive nitrogen species enhance fibrosis and pancreatic tumor growth in vivo. (*A*) Masson's trichrome stain, (*B*) Picrosirius red stain, and (*C*) Vimentin immunofluorescence (orange) and nuclei (blue) in sections from tumors implanted with KPC pancreatic cancer cells alone (−) or coimplanted with murine pancreatic stellate cells cultured in complete medium (mPSC) or conditioned medium from BMDMs treated with 1400W + PBS (1400W CTL CM mPSC), 1% gelatin (GEL CM mPSC), or 1400W + 1% gelatin (1400W GEL CM mPSC) for 24 h prior to injecting cells subcutaneously into the rear flanks of nude mice. For all graphs, values are mean ± SE $n = 8$ mice. All fluorescent images quantified in arbitrary units and presented relative to values obtained for control. Statistical significance was determined using a one-way ANOVA test. Adjusted P values for two group comparisons are plotted. *$P < 0.05$; **$P < 0.001$; ***$P < 0.0001$; ns, not significant.

cellular phenotypes and molecular functions of immune cells within the tumor microenvironment can be profoundly influenced by collagen content and architecture. For example, high collagen density has been shown to promote the acquisition of an immunosuppressive phenotype by macrophages (49). High-density collagen matrix has been also shown to reduce T cell proliferation and down-regulate T cell cytotoxic activity (50). Thus, the profibrinogenic circuit described in this study could directly contribute to the immune evasive properties of pancreatic cancer and may inform future immune intervention strategies.

Materials and Methods

Cell Lines, Primary Cells, and Cell Culture Treatments. All cells were maintained under 5% CO_2 at 37 °C and cultured in DMEM (Gibco) supplemented with 10% FBS (Gibco), penicillin and streptomycin (Gibco) (complete media). BMDMs were isolated from wild-type C57BL/6 mice (Charles River Laboratories) or *Mrc1*-null mice (B6.129P2-Mrc1tm1Mnz/J, Jackson Laboratories), and differentiated with 10 ng/mL recombinant murine M-CSF (Peprotech 315-02) for 4 to 7 d. For M1 polarization, differentiated BMDMs were treated with 20 ng/mL LPS (Sigma, L2630) for 24 h. For all other experiments, differentiated BMDMs were treated with 20 ng/mL recombinant mouse IL-4 (R&D Systems, 404-ML-010) for 24 h. Where indicated, differentiated BMDMs were treated with 10 ng/mL recombinant murine IL-13 (Peprotech 210-13) or 10 ng/mL recombinant murine IL-10 (Peprotech 210-10). Mouse *KPC* (4662) pancreatic cancer cells (51) and murine PSCs (mPSC) (52) were derived as previously described. Primary PSCs were harvested from the pancreata of wild-type C57BL/6J mice.

Gelatin (Bio-Rad 170-6537) treatments were diluted 1% in complete DMEM, as described above, for 24 h. The following sources and concentrations were used for chemicals: 50 nM BafA (Cayman Chemical, 88899-55-2), 5 mM MDLA (Sigma, M6001), 100 μM 1400W (Santa Cruz, sc3564), and 0.4 mM DPTA NON-Oate (Santa Cruz, sc202144). Oregon Green 488 conjugate-labeled gelatin (OG gelatin) was purchased from Invitrogen (G13186). DQ collagen was purchased from Molecular Probes (D1260). Soluble nitrite and total nitrate were quantified in conditioned medium samples using a Total Nitric Oxide and Nitrate/Nitrite kit (R&D Systems KGE001), according to the manufacturer's protocol.

Control (Dharmacon siGENOME Non-Targeting siRNA Pool #2 D-001206-14-20) or *Mrc1* (Dharmacon SMARTpool:siGENOME Mrc1 siRNA M-047522-00-0005) siRNA was transfected into cells using Lipofectamine RNAiMAX Transfection Reagent (Thermo Fisher Scientific 13778100) according to the manufacturer's protocol. BMDMs were plated in a 12-well plate and transfected with 100 nM siRNA twice over 7 d before experimentation.

Antibodies. Antibodies used for Western blotting are as follow: mouse anti-α-tubulin (Sigma T5168), rabbit anti-Mannose receptor (Abcam ab64693), rabbit anti-Arginase 1 (Cell Signaling 9819S), mouse anti-iNOS (Mouse Specific; Cell Signaling 2982). Monoclonal antibodies used for flow cytometry were all purchased from BioLegend unless indicated: anti-CD45 (FITC-anti-mouse-CD45, clone 30-F11), anti-F480 (PE/Cy7-anti-mouse F4/80, clone BM8), anti-Ly6C (Brilliant violet 421-anti-mouse Ly-6C, clone HK1.4), anti-CD206/MRC1 (FITC-anti-mouse-CD206, clone C068C2), anti-iNOS (APC-anti-mouse-NOS2, clone CXNFT), and anti-ARG1 (PE-anti-h/mArginase 1, clone 658922, R&D Systems). COL1A1 antibody used for in vitro indirect immunofluorescence staining (Abcam, rabbit anti-collagen 1, amino acids 1 to 1464, ab34710) was used at a concentration of 2 ng/mL Intracellular COL1A1 was detected with methanol fixation and permeabilization. Extracellular COL1A1 was detected with paraformaldehyde fixation

and no permeabilization. For in vivo staining, F4/80 antibody (rat anti-F4/80, Abcam, clone A3-1, ab6640) was used at a concentration of 1:150, Vimentin antibody (goat anti-rabbit, Cell Signaling, 57415) was used at a concentration of 1:100, CD68 antibody (DAKO, KP1) was used at a concentration of 1:75, CK19 antibody (Biocare, Ks19.1) was used at 1:100, iNOS antibody (Novus, nb300-605) was used at 1:400, and ARG1 antibody was used at 1:500. Murine tissue staining was done by standard immunofluorescence staining. Human tissue staining was done using Vectra 3 OPAL multiplex high-throughput immunohistochemistry at the New York University School of Medicine Histopathology Core Facility.

Collagen Uptake and Degradation Assays. For in vitro assays, cells were seeded on glass coverslips 24 to 48 h before the assay. Coverslips were then removed and placed cell-side down onto a drop solution of 0.1 mg/mL OG gelatin or DQ collagen in serum-free medium. After a 30-min incubation under standard culture conditions, cells were rinsed three times with ice-cold PBS and fixed with 3.7% formaldehyde solution in PBS (Gibco). Coverslips were counterstained with DAPI (Sigma) and mounted on glass slides using DAKO mounting medium (DAKO). For drug treatment, cells were preincubated with BafA at the dosage noted above for 3 h prior to the start of the assay. Images were obtained using Axiovert 200 inverted fluorescent microscope (Zeiss) or TiE2 Eclipse inverted microscope (Nikon) and quantified, as previously described (53).

Gene Expression Analysis. For qPCR analysis, total RNA was harvested using the Qiagen RNA extraction Kit (Qiagen). Purified RNA (1 μg) was reverse-transcribed using the QuantiTect Reverse Transcription kit (Qiagen). Specific transcripts were amplified by Power SYBR Green PCR Master Mix (Applied Biosystems) using a Stratagene Mx 3005P thermocycler and analyzed using ΔCT method to quantify gene expression. Primers were obtained from Integrated DNA Technologies (IDT) with the following sequences (5'-3'): Gapdh (forward) CACGGCAAATTCAACGGCACAGTG, (reverse) ACCCGTTTGGCTCCACCCTTCA; iNos (forward) GTTCTCAGCCCAACAATACAAGA, (reverse) GTGGACGGGTCGATGTCA; Arg1 (forward) GTGAAGAACCCACGGTCTGT, (reverse) GCACCACACTGACTCTTCCA; Mrc1 (forward) GGGCAGTCACCATATTTATTGGC, (reverse) GCAAAGTTGGGTTCTCCTGTAGCC; Rps29 (forward) GTCTGATCCGCAAATACGGG, (reverse) AGCCTATGTCCTTCGCGTACT; Hsp47 (forward) AAGATGCAGAAGAAGGCTGTC, (reverse) CTGTGACACCCCTGAATTTGGT; αSma (forward) ATAACCCTTCAGCGTTCAGC, (reverse) CACGATGGATGGGAAAACAG; Ctgf (forward) AGTGTGCACTGCCAAAGATG, (reverse) CCAGGCAAGTGCATTGGTAT; Cdh10 (forward) AGTAGTCCTCTTTGCAGCCC, (reverse) GCGTAGGTAGCCAGTGAGTC; Col1a1 (forward) AGACATCCCACCAATCACCTG, (reverse) GGCAGTTCTTGGTCTCGTCAC; Col2a1 (forward) ATGAGGGGAGCGGTAGAGACC, (reverse) GCCCTAATTTTCGGGCATCC; Col3a1 (forward) GCCCACAGCCTTCTACAC, (reverse) CCAGGGTCACCATTTCTC; Col4a1 (forward) TATCTCTGGGGACAACATCCG, (reverse) CATCTCGCTTCTCTCTATGGT.

Western Blot Analysis. Total cell lysates were harvested in sample buffer (40 mmol/L Tris, pH 6.8, 1% SDS, 5% β-mercaptoethanol, 7.5% glycerol, and 0.01% bromophenol blue) and incubated at 95 °C for 5 min. Cell lysates were loaded onto 10% SDS/PAGE and transferred onto nitrocellulose membranes for 1 h at 100 V at 4 °C. Membranes were blocked for 1 h at room temperature in 3% BSA (Sigma Aldrich) diluted in PBS containing 0.1% Tween-20 prior to immunodetection.

Flow Cytometry Analysis. Staining for flow cytometry analysis was performed by incubating single-cell suspensions with primary fluorochrome-labeled antibodies on ice for 30 min. Zombie Yellow Fixable Viability Kit (BioLegend 423103) was used to assess live/dead populations. Cells were fixed in 3.7% formaldehyde diluted in FACs buffer (PBS + 5% FBS) for 30 min at room temperature prior to analysis. For iNOS and ARG1 staining, cells were permeabilized and fixed with FoxP3/Transcription Factor Staining Buffer Set (eBioscience CNOO-5523) for 30 min at room temperature and stained overnight at 4 °C. All samples were washed once with FACs buffer prior to analysis on an LSRII HTS flow cytometer (BD Biosciences). Collected data were analyzed using FlowJo data analysis software (v10).

Polar Metabolite Extraction and GC-MS Analysis of Arginine. IL-4-treated BMDMs were treated with 1% dialyzed gelatin for 24 h in amino acid free DMEM (US Biological Life Sciences) supplemented with ^{13}C-labeled L-arginine and all other unlabeled amino acids at the concentrations normally found in

regular DMEM (Gibco), 10% dialyzed FBS (Gibco), and 1% penicillin and streptomycin (Gibco). Polar metabolites from BMDM cell pellets were extracted by adding 500 μL HPLC-grade methanol (−20 °C) and 200 μL HPLC-grade water (4 °C) containing 1 nmol of $^{13}C_6,^{15}N_4$-labeled arginine (Cambridge Isotope Laboratories) to each sample. Samples were vigorously vortexed at 4 °C for ~10 to 15 min until cell pellet was dissociated. Next, 500 μL HPLC-grade chloroform (−20 °C) was then added to each sample followed by vortexing for 10 to 15 min and cold centrifugation; 400 μL of supernatant containing polar metabolites was transferred to new tubes and immediately dried by using a SpeedVac (Savant Thermo SPD111V) for downstream derivatization and gas chromatography-mass spectrometry (GC-MS) analysis.

Arginine spontaneously transforms into ornithine using standard methoxime tert-butyldimethylsilyl (tBDMS) derivatization (54) preventing accurate quantification. To prepare samples for GC-MS analysis, we derivatized arginine to its trifluoroacetyl derivative. Briefly, 40 μL of N-methyl-bis(trifluoroacetamide) (N-MBTFA, Sigma) was added to each dried sample and incubated at 70 °C with for 60 to 90 min with vortexing every 5 to 10 min. Samples were briefly centrifuged to remove insoluble material, and 30 μL of clarified sample was transferred to sample vials for GC-MS analysis.

Trifluoroacetylated arginine derivatives were analyzed by GC-MS using a DB-35MS column (30 m × 0.25 mm i.d. × 0.25 μm) installed in an Agilent 5977B gas chromatograph interfaced with an Agilent 5977B mass spectrometer. The GC temperature was held at 75 °C after injection for 3 min, ramped to 225 °C at 10 °C/min, held at 225 °C for 5 min, and postrun held at 320 °C for 2 min. The MS detector was operated in selected ion monitoring mode over a range of 375 to 388 m/z. Under these conditions, 2,3,4,5-tetrakis(trifluoroacetyl)arginine eluted at ~14 to 16 min with a main fragment ion of 375 m/z representing [M-183; -CF3 –C2F3O –OH] with a formula of $C_{11}H_9N_4O_4F_6$. Ion abundances for M+0 (375 m/z) representing unlabeled arginine present in BMDM samples and M+10 (385 m/z) representing the internal isotopically labeled standard (1 nmol) were quantified using in-house algorithms customized to incorporate fluorinated analytes. As an external control, 5 μL of DMEM (Gibco) containing 0.4 mM arginine was extracted alongside each batch of independently collected samples and quantified as a quality control. The absolute abundance of arginine in BMDMs was quantified, as previously described (55).

Peroxynitrite Detection. Peroxynitrite production by gelatin-fed macrophages was evaluated using a two-photon, ratiometric fluorescent probe (56). Macrophages were treated with iNOS inhibitor 1400W at the dosage indicated above for 3 h in complete DMEM. Thereafter, 1% gelatin was added directly to the media for 24 h. Cells were then incubated with 10 μM probe for 1 h in imaging medium (Fluorobrite DMEM, Thermofisher A1896701), and then imaged live at 37 °C using a Zeiss LSM 880 laser scanning confocal microscope with a 63× N.A. 1.4 lens. Peroxynitrite oxidizes the recognition part of an energy acceptor on the probe, triggering a shift of fluorescence from 476 nm to 574 nm when excited at 405 nm. Peroxynitrite generated was determined by quantifying the fluorescence intensity shift from 476 to 574 nm.

OPAL IHC Analysis. Semiautomated image acquisition was performed on Vectra3 multispectral imaging (MSI) system. After whole-slide scanning at 20×, the tissue was manually outlined to select fields for spectral unmixing. InForm v2.4.10 software from Akoya Biosciences was used for spectral unmixing and image analysis.

The following MSI analysis fields were used for analysis (Table 1): Cells were segmented based on nuclear signal (DAPI). Cells were phenotyped after segmentation using inForm's trainable algorithm based on glmnet package in R. Four algorithms were created to classify cell as CD68+ or "other," CK19+ or "other," Arg1+ or "other," and iNos+ or "other." Phenotypes were reviewed for different samples during training iterations. Data were exported as text containing sample names, field of acquisition coordinates, individual cell information including coordinates, and identified phenotype. Each image was analyzed with all four algorithms so that every cell was classified four times. Concatenation of all phenotyping information was performed in using the Phenoptr Reports package (57) in RStudio software (58).

Conditioned Medium Experiments. IL-4–treated BMDMs derived and treated with 1% gelatin ± 1400W, as described above, were placed in fresh gelatin-free DMEM (Gibco) + 10% FBS for 3 h. Conditioned medium was harvested, filtered

Table 1. Multispectral imaging fields used for analysis

Slide ID	No. fields	Total cells	Scanned on
111119-1654-all	25	46,235	Vectra 3
111119-379-all	89	145,653	Vectra 3
111119-753-all	84	114,959	Vectra 3

(0.2 μm), and placed on mPSCs for 24 h at 37 °C prior to harvesting for functional analyses.

Animal Studies. For macrophage profiling experiments, the entire pancreas from 3-mo-old male and female *KPC* GEMM mice was collected. For orthotopic implantations, 1×10^5 *KPC* cells were resuspended in 20 μL cold PBS and mixed with 20 μL Matrigel (Corning 354234) prior to injection into the pancreas of wild-type 8-wk-old female C57BL/6 mice (CRL). Tumors from orthotopically implanted mice were harvested after 2 wk. Tissue from both *KPC* GEMM mice and *KPC* orthotopics were digested with 1.25 mg/mL collagenase type IV (Worthington LS004188)/0.1% soy bean trypsin inhibitor (Sigma-Aldrich T6522) for flow cytometry analysis.

For graft assays, 8- to 10-wk-old female wild-type or *Mrc1* null mice (B6.129P2-*Mrc1*^{tm1Mnz}/J, Jackson Laboratories) were injected subcutaneously into the flanks with 250,000 *KPC* pancreatic cancer cells in 100 μL of a 1:1 PBS/Matrigel solution. Once tumors reached ~300 mm^3, they were injected with OG-gelatin solution (1 mg/mL). Four hours after injection, tumors were harvested, embedded, and frozen in OCT compound (Tissue-Tek). Following cryosectioning, slides were stained with DAPI and imaged using an Axiovert 200 inverted fluorescent microscope. F4/80 staining was used to mark macrophages; green puncta were counted within F4/80$^+$ cells using ImageJ.

For tumor coimplantations, 2.5×10^5 *KPC* cells $\pm$ conditioned medium–treated 1.25×10^6 mPSCs were resuspended in 40 μL cold PBS and mixed with 40 μL Matrigel (Corning 354234) prior to subcutaneous injection into the rear flanks of wild-type 6- to 8-wk-old female NCr nude mice (Taconic NCR/NU). One tumor was implanted per flank. Tumors were harvested after 2 wk and measured using a standard caliper (Fisher Scientific) over the 2-wk period. Tumors were fixed overnight in 10% formalin (Fisher) and processed for paraffin-embedding. Sirius red staining was performed using a Picrosirius Red Stain Kit (Polysciences 24901), and Masson's trichrome staining was performed at the New York University School of Medicine Histopathology Core Facility. Histology images were quantified using ImageJ. For Picrosirius red stain quantification, a minimal intensity threshold was used to eliminate background and then fiber density was measured as image percent area coverage. Five images per tumor stained were acquired. For Masson's trichrome stain quantification, RGB images were deconvolved and the minimal intensity threshold was used to eliminate background in the blue channel. Fiber density was measured as image percent area coverage. Ten images per tumor type stained were acquired. Images used in quantification were all of similar composition percent tissue area per frame. All mice were euthanized using CO_2 and subsequent cervical dislocation at the time of harvesting tissue for analysis (59). All animal care and procedures were approved by the Institutional Animal Care and Use Committee at the New York University School of Medicine.

Statistical Analyses. Statistical comparisons were evaluated by either Student's *t* test or one-way ANOVA using Prism (GraphPad) unless noted otherwise.

Data Availability. All unique reagents generated in this study are available from the corresponding author with a completed Materials Transfer Agreement. All study data are included in the main text and *SI Appendix*.

Author affiliations: aVilcek Institute of Graduate Biomedical Sciences, New York University Grossman School of Medicine, New York, NY 10016; bDepartment of Biochemistry and Molecular Pharmacology, New York University Grossman School of Medicine, New York, NY 10016; cMicroscopy Core, Division of Advanced Research Technologies, New York University Grossman School of Medicine, New York, NY 10016; and dDepartment of Radiation Oncology, New York University Medical Center, New York, NY 10016

Author contributions: M.M.L., S.P., J.P., M.C., and D.B.-S. designed research; D.B.-S. directed the study; M.M.L., S.P., J.P., and M.C. performed research; M.M.L., S.P., J.P., M.C., A.C.K., and D.B.-S. analyzed data; and M.M.L. and D.B.-S. wrote the paper.

Reviewers: F.M., The University of Texas MD Anderson Cancer Center; and E.W., Rutgers the State University of New Jersey.

1. American Cancer Society, *Cancer Facts & Figures 2021* (American Cancer Society, Atlanta, 2021).
2. A. Neesse *et al.*, Stromal biology and therapy in pancreatic cancer. *Gut* **60**, 861–868 (2011).
3. H. Salmon *et al.*, Matrix architecture defines the preferential localization and migration of T cells into the stroma of human lung tumors. *J. Clin. Invest.* **122**, 899–910 (2012).
4. D. Xie, K. Xie, Pancreatic cancer stromal biology and therapy. *Genes Dis.* **2**, 133–143 (2015).
5. D. J. Bulle, S. van der Merwe, E. Van Cutsem, C. Verslype, J. J. van Pelt, Relevance of the stroma in pancreatic ductal adenocarcinoma and its challenges for translational research. *J. Cancer Treatment Diagn.* **2**, 1–15 (2017).
6. T. Stylianopoulos, L. L. Munn, R. K. Jain, Reengineering the physical microenvironment of tumors to improve drug delivery and efficacy: From mathematical modeling to bench to bedside. *Trends Cancer* **4**, 292–319 (2018).
7. E. Karamitopoulou, Tumour microenvironment of pancreatic cancer: Immune landscape is dictated by molecular and histopathological features. *Br. J. Cancer* **121**, 5–14 (2019).
8. D. Thomas, P. Radhakrishnan, Tumor-stromal crosstalk in pancreatic cancer and tissue fibrosis. *Mol. Cancer* **18**, 14 (2019).
9. W. J. Ho, E. M. Jaffee, L. Zheng, The tumour microenvironment in pancreatic cancer–Clinical challenges and opportunities. *Nat. Rev. Clin. Oncol.* **17**, 527–540 (2020).
10. H. F. Dvorak, Tumors: Wounds that do not heal–Redux. *Cancer Immunol. Res.* **3**, 1–11 (2015).
11. D. S. Foster, R. E. Jones, R. C. Ransom, M. T. Longaker, J. A. Norton, The evolving relationship of wound healing and tumor stroma. *JCI Insight* **3**, e99911 (2018).
12. Y. Hua, G. Bergers, Tumors vs. chronic wounds: An immune cell's perspective. *Front. Immunol.* **10**, 2178 (2019).
13. M. V. Apte, J. S. Wilson, A. Lugea, S. J. Pandol, A starring role for stellate cells in the pancreatic cancer microenvironment. *Gastroenterology* **144**, 1210–1219 (2013).
14. D. von Ahrens, T. D. Bhagat, D. Nagrath, A. Maitra, A. Verma, The role of stromal cancer-associated fibroblasts in pancreatic cancer. *J. Hematol. Oncol.* **10**, 76 (2017).
15. L. Monteran, N. Erez, The dark side of fibroblasts: Cancer-associated fibroblasts as mediators of immunosuppression in the tumor microenvironment. *Front. Immunol.* **10**, 1835 (2019).
16. C. Frantz, K. M. Stewart, V. M. Weaver, The extracellular matrix at a glance. *J. Cell Sci.* **123**, 4195–4200 (2010).
17. E. Henke, R. Nandigama, S. Ergün, Extracellular matrix in the tumor microenvironment and its impact on cancer therapy. *Front. Mol. Biosci.* **6**, 160 (2020).
18. D. H. Madsen *et al.*, The non-phagocytic route of collagen uptake: A distinct degradation pathway. *J. Biol. Chem.* **286**, 26996–27010 (2011).
19. D. H. Madsen *et al.*, M2-like macrophages are responsible for collagen degradation through a mannose receptor-mediated pathway. *J. Cell Biol.* **202**, 951–966 (2013).
20. K. Ley, M1 means kill; M2 means heal. *J. Immunol.* **199**, 2191–2193 (2017).
21. A. Shapouri-Moghaddam *et al.*, Macrophage plasticity, polarization, and function in health and disease. *J. Cell. Physiol.* **233**, 6425–6440 (2018).
22. M. Orecchioni, Y. Ghosheh, A. B. Pramod, K. Ley, Macrophage polarization: Different gene signatures in M1(LPS+) vs. classically and M2(LPS−) vs. alternatively activated macrophages. *Front. Immunol.* **10**, 1084 (2019).
23. A. C. Thomas, J. T. Mattila, "Of mice and men": Arginine metabolism in macrophages. *Front. Immunol.* **5**, 479 (2014).
24. M. Rath, I. Müller, P. Kropf, E. I. Closs, M. Munder, Metabolism via arginase or nitric oxide synthase: Two competing arginine pathways in macrophages. *Front. Immunol.* **5**, 532 (2014).
25. D. S. Lind, Arginine and cancer. *J. Nutr.* **134**(10, suppl.), 2837S–2841S, discussion 2853S (2004).
26. M. Jahani, F. Noroznezhad, K. Mansouri, Arginine: Challenges and opportunities of this two-faced molecule in cancer therapy. *Biomed. Pharmacother.* **102**, 594–601 (2018).
27. S. El-Gayar, H. Thüring-Nahler, J. Pfeilschifter, M. Röllinghoff, C. Bogdan, Translational control of inducible nitric oxide synthase by IL-13 and arginine availability in inflammatory macrophages. *J. Immunol.* **171**, 4561–4568 (2003).

28. M. R. Sullivan et al., Quantification of microenvironmental metabolites in murine cancers reveals determinants of tumor nutrient availability. eLife 8, e44235 (2019).

29. D. D. Thomas et al., The chemical biology of nitric oxide: Implications in cellular signaling. Free Radic. Biol. Med. 45, 18–31 (2008).

30. J. R. Lancaster Jr, Nitric oxide: A brief overview of chemical and physical properties relevant to therapeutic applications. Future Sci. OA 1, FSO59 (2015).

31. K. Obayashi, H. Akamatsu, Y. Okano, K. Matsunaga, H. Masaki, Exogenous nitric oxide enhances the synthesis of type I collagen and heat shock protein 47 by normal human dermal fibroblasts. J. Dermatol. Sci. 41, 121–126 (2006).

32. C. Chandler, T. Liu, R. Buckanovich, L. G. Coffman, The double edge sword of fibrosis in cancer. Transl. Res. 209, 55–67 (2019).

33. J. Winkler, A. Abisoye-Ogunniyan, K. J. Metcalf, Z. Werb, Concepts of extracellular matrix remodelling in tumour progression and metastasis. Nat. Commun. 11, 5120 (2020).

34. O. Olivares et al., Collagen-derived proline promotes pancreatic ductal adenocarcinoma cell survival under nutrient limited conditions. Nat. Commun. 8, 16031 (2017).

35. Z. Zhu et al., Tumour-reprogrammed stromal BCAT1 fuels branched-chain ketoacid dependency in stromal-rich PDAC tumours. Nat. Metab. 2, 775–792 (2020).

36. M. B. Witte, F. J. Thornton, D. T. Efron, A. Barbul, Enhancement of fibroblast collagen synthesis by nitric oxide. Nitric Oxide 4, 572–582 (2000).

37. R. Urtasun, L. Conde de la Rosa, N. Nieto, Oxidative and nitrosative stress and fibrogenic response. Clin. Liver Dis. 12, 769–790, viii (2008).

38. K. Yamasaki et al., Reversal of impaired wound repair in iNOS-deficient mice by topical adenoviral-mediated iNOS gene transfer. J. Clin. Invest. 101, 967–971 (1998).

39. J. D. Luo, Y. Y. Wang, W. L. Fu, J. Wu, A. F. Chen, Gene therapy of endothelial nitric oxide synthase and manganese superoxide dismutase restores delayed wound healing in type 1 diabetic mice. Circulation 110, 2484–2493 (2004).

40. Y. Vodovotz et al., Regulation of transforming growth factor beta1 by nitric oxide. Cancer Res. 59, 2142–2149 (1999).

41. S. Akool et al., Nitric oxide induces TIMP-1 expression by activating the transforming growth factor beta-Smad signaling pathway. J. Biol. Chem. 280, 39403–39416 (2005).

42. D. Tang et al., Persistent activation of pancreatic stellate cells creates a microenvironment favorable for the malignant behavior of pancreatic ductal adenocarcinoma. Int. J. Cancer 132, 993–1003 (2013).

43. J. Zent, L. W. Guo, Signaling mechanisms of myofibroblastic activation: Outside-in and inside-out. Cell. Physiol. Biochem. 49, 848–868 (2018).

44. T. Ichikawa et al., Peroxynitrite augments fibroblast-mediated tissue remodeling via myofibroblast differentiation. Am. J. Physiol. Lung Cell. Mol. Physiol. 295, L800–L808 (2008).

45. C. Szabó, H. Ischiropoulos, R. Radi, Peroxynitrite: Biochemistry, pathophysiology and development of therapeutics. Nat. Rev. Drug Discov. 6, 662–680 (2007).

46. D. Öhlund et al., Distinct populations of inflammatory fibroblasts and myofibroblasts in pancreatic cancer. J. Exp. Med. 214, 579–596 (2017).

47. D. A. Tuveson, Fighting the sixth decade of the cancer war with better cancer models. Cancer Discov. 11, 801–804 (2021).

48. M. Egeblad, M. G. Rasch, V. M. Weaver, Dynamic interplay between the collagen scaffold and tumor evolution. Curr. Opin. Cell Biol. 22, 697–706 (2010).

49. A. M. H. Larsen et al., Collagen density modulates the immunosuppressive functions of macrophages. J. Immunol. 205, 1461–1472 (2020).

50. D. E. Kuczek et al., Collagen density regulates the activity of tumor-infiltrating T cells. J. Immunother. Cancer 7, 68 (2019).

51. A. Lo et al., Tumor-promoting desmoplasia is disrupted by depleting FAP-expressing stromal cells. Cancer Res. 75, 2800–2810 (2015).

52. C. M. Sousa et al., Pancreatic stellate cells support tumour metabolism through autophagic alanine secretion. Nature 536, 479–483 (2016).

53. C. Commisso et al., Macropinocytosis of protein is an amino acid supply route in Ras-transformed cells. Nature 497, 633–637 (2013).

54. G. E. Corso, M. Gallo, A. Dello Russo, Transformation of arginine into ornithine during the preparation of its tert-butyldimethylsilyl derivative for analysis by gas chromatography/mass spectrometry. Biol. Mass Spectrom. 22, 698–702 (1993).

55. S. J. Parker et al., Selective alanine transporter utilization creates a targetable metabolic niche in pancreatic cancer. Cancer Discov. 10, 1018–1037 (2020).

56. S. Chen et al., Two-photon, ratiometric, quantitative fluorescent probe reveals fluctuation of peroxynitrite regulated by Arginase 1. Anal. Chem. 93, 10090–10098 (2021).

57. K. S. Johnson (2020) phenoptr: inForm Helper Functions. R package version 0.3.2. https://akoyabio.github.io/phenoptr/.

58. R. Team, RStudio: Integrated Development for R (RStudio, Inc., Boston, MA, 2015).

59. National Research Council, Guide for the Care and Use of Laboratory Animals (National Academies Press, Washington, DC, ed. 8, 2011).